Received: 23 August 2023 | Revised: 24 October 2023 | Accepted: 8 November 2023

DOI: 10.1111/jace.19597

Journal of the American Ceramic Society

RESEARCH ARTICLE

# Effect of sintering temperature on the dielectric properties of 3D-printed alumina ($Al_2O_3$) in the W-band

**Kai-Daniel Jenkel**[1] | **Jesús Sánchez-Pastor**[2] | **Mohammad Mahdi Baloochian**[1] | **Rolf Jakoby**[2] | **Masoud Sakaki**[1] | **Alejandro Jiménez-Sáez**[2] | **Niels Benson**[1]

[1]Institute of Technology for Nanostructures and CENIDE, University of Duisburg-Essen, Duisburg, Germany

[2]Institute of Microwave Engineering and Photonics, Technische Universität Darmstadt, Darmstadt, Germany

**Correspondence**
Masoud Sakaki and Niels Benson, Institute of Technology for Nanostructures and CENIDE, University of Duisburg-Essen, 47057 Duisburg, Germany.
Email: masoud.sakaki@uni-due.de and niels.benson@uni.due.de

**Funding information**
German Research Foundation, Grant/Award Number: CRC/TRR 196 MARIE

**Abstract**

This contribution discusses the impact of sintering temperatures on dielectric properties of 3D-printed alumina ($Al_2O_3$) in the W-band, by evaluating high quality factor ($-Q$) resonators integrated in a 2D photonic crystal structure. By varying the sintering temperature of the lithography-based ceramic manufactured (LCM) samples, the microstructure of the material can be defined, which has a direct impact on the dielectric permittivity and material losses. Using a highly accurate photonic crystal structure, with a dimensional variation below 2% from print to print, an accurate extraction and evaluation of the dielectric material properties could be achieved. The relative permittivity of the alumina was tuned from 4.4 at 1250°C to 9.2 at 1650°C, whereas the observed change in dielectric losses was moderate. The maximum in observed dielectric loss for samples sintered at the lowest evaluated temperature, only yields an average value of $30 \times 10^{-4}$. This demonstrates the versatility of the LCM technology for mm- and sub-mm-wave applications and its possibilities for material tuneability.

**KEYWORDS**

additive manufacturing, alumina, dielectric loss, dielectric materials/properties, permittivity, sinter/sintering

## 1 | INTRODUCTION

Additive manufacturing (AM) has made tremendous progress in recent years and has found its way into a wide variety of technological fields, ranging from prototyping, over medical applications to space applications.[1–4] The reason for this is the advantage over traditional manufacturing methods in terms of complex design, fast fabrication, and low-cost production.[5] The production of 3D-printed ceramics is more complex, compared to other materials, such as polymers or metals.[6] Especially the post-treatment, which can consist of multiple steps, is very demanding. Moreover, the implementation for high resolution, good surface quality, and specific mechanical properties is challenging.[2] For this reason, many different approaches for ceramic additive fabrication are being developed, whereas a few processing methods are already well established, both in industry and research. A distinction of the different technologies can be made based on the starting material and the required processing steps.

Materials wise, various ceramics (e.g., oxides, carbides, nitrides, and apatites) have been intensively investigated and adopted for ceramic additive fabrication.[7–12] Especially, due to high market demand, alumina is available for commercial-level AM.

From a processing type point of view, an established process for ceramic additive fabrication is the slurry-based approach, which offers numerous processing possibilities, such as vat-photopolymerization.[13] This principle is used in the lithography-based ceramic manufacturing (LCM) method, where a digital light processing (DLP)-projector is used to create a pixel pattern in a layer of slurry containing a mixture of photocurable polymers and fine ceramic powders.[14] The absorption of the light triggers photopolymerization in the slurry, creating a 3D-polymer network in a layer-by-layer process, in which the solid ceramic particles are fixed.[14] Subsequent cleaning and thermal post-processing steps convert the printed green body into the desired ceramic, for which high densities (>99%) and a low surface roughness ($R_a < 0.4\ \mu$m) can be obtained.[15] Furthermore, a high structural resolution in the sub 200 $\mu$m range is possible.

Promising dielectric properties of $Al_2O_3$, combined with the high accuracy of the LCM-method, make LCM-printed alumina parts particularly attractive for the field of high frequency technology.[16] Examples are as follows: corner reflectors with an enhanced radar cross section,[17,18] high-$Q$ resonators based on photonic crystal structure (unloaded $Q$ of 2601),[19–21] and Luneburg lenses with a maximum gain of 16.51 dBi.[22] However, for the successful design and implementation of LCM-printed alumina-based high frequency devices, accurate information about the dielectric material/part properties (i.e., permittivity and loss factor) is crucial.

Therefore, in this contribution, the effect of the sintering temperature on the dielectric properties of LCM-printed $Al_2O_3$ in the W-band is evaluated. For this purpose, in a first step, the shrinkage factors during temperature treatment are determined for various sintering temperatures. This knowledge is then used to manufacture several high-$Q$ resonators, which are sintered at different temperatures but are designed to have identical sizes. Afterward, the resonator performance is experimentally evaluated, and the dielectric properties are extracted via comparison of simulation and measurement. To correlate the observed change in dielectric material properties with the microstructure of the ceramic, an investigation via scanning electron microscopy (SEM) and the application of different classical models (Looyenga, Bruggeman, and Böttcher)[23–25] is employed.

## 2 | EXPERIMENTAL PROCEDURES

### 2.1 | Design of high-$Q$ resonators

To investigate the impact of sintering temperature/material quality variation on high-performance mm-wave devices, and to be able to extract dielectric material information, an alumina high-$Q$ resonator is used as an example structure based on the model presented in the literature.[26] The structure is a fully dielectric photonic crystal, which consists of a periodic permittivity variation with a specific period (also known as the lattice). In our case, this variation is achieved by embedding air holes ($\varepsilon_r = 1$) into alumina ($\varepsilon_r$ dependent on sintering temperature), as illustrated in Figure 1. With this configuration, a frequency-dependent EM bandgap is engineered, through which an incoming wave of a certain frequency range is not able to propagate, which is the host of the high-$Q$ resonator by locally modifying the photonic crystal lattice. The software CST Studio Suite was used to design the structure of the resonator and to simulate the dielectric properties of the device.

### 2.2 | Fabrication

This contribution focuses on alumina devices, produced with a CeraFab 7500 from Lithoz GmbH. The LCM technology is a slurry-based approach, for which the Lithalox 360 slurry was used. This is a commercial slurry based on submicron ceramic particles with a content of 49 vol% and a viscosity of 6.5 Pa s at a shear rate of 10 $s^{-1}$ (values taken from manufacturer), developed for the printing of delicate structures.[27] A DLP-projector (@ wavelength: ~450 nm) is used to create a pixel pattern with a pixel resolution of $25 \times 25\ \mu m^2$. The energy per layer can be adjusted by the software of the printer and influences the accuracy, as well as the stability of the print. For high stability and accuracy, an exposure time of 4.1 s per layer at an energy of 410 mJ/$cm^2$ was applied to fabricate the green body in a layer-by-layer approach. For the design of the resonator prints, different shrinkage factors (determined by evaluating simple blocks) were considered to account for the shrinkage during the temperature post treatment.

After printing a cleaning step is necessary, which is done by applying LithaSol 20, a special fluid based on organic esters inert to the polymers used to remove unpolymerized residues. After cleaning a temperature post treatment is needed for the transition of the green body into a ceramic part. This involves an initial slow drying process up to 140°C, followed by a debinding step where the polymers

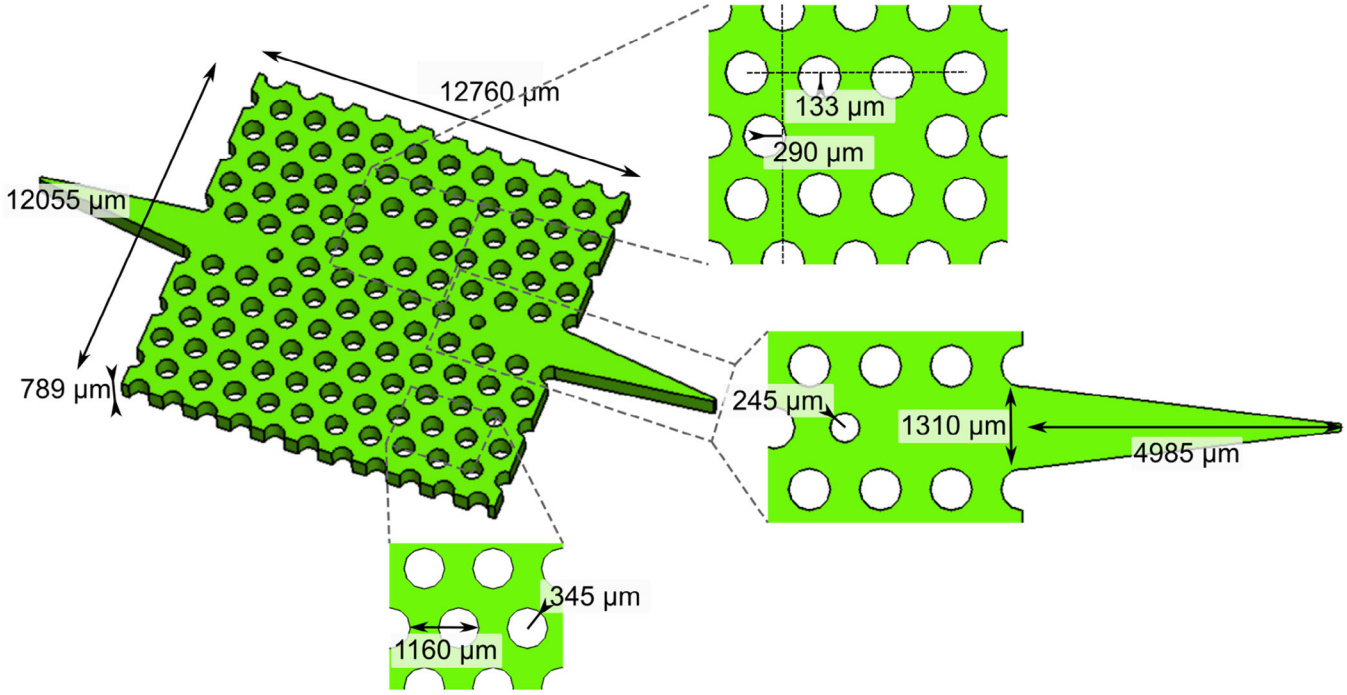


**FIGURE 1** Schematic illustration of the designed photonic crystal high-*Q* resonator.

in the green body structure are decomposed into volatile carbon containing groups such as $CO_2$ at temperatures up to 1100°C and low heating rates in the order of 1 K/min (based on TGA and DSC measurement conducted by Schwentenwein and Homa[15]). The subsequent and final step to densify the ceramic is sintering at high temperatures (e.g., 1650°C) with heating rates in the 0.8 K/min range. This maximum temperature is maintained for 2 h before cooling down is initiated. The cooling rate down to a temperature of 1200°C is 0.83 K/min, which is increased to a rate of 1.6 K/min for the temperature range of 1200°C—room temperature. The debinding and sintering steps were done in the same oven using ambient atmosphere. For this work, different sintering processes were applied to vary the sample density and thus the effective sample permittivity. To accomplish this, the maximum temperature was varied in 100°C steps between 1250 and 1650°C. The different total temperature processes are summarized in Supplementary A (Figure S1).

## 2.3 | Characterization

Microstructure: Blocks with the same size ($6 \times 4 \times 3$ mm$^3$) were printed and sintered at different temperatures and used to determine the shrinkage factor and density in dependence of post-processing temperature. Densities of the blocks were obtained by gravimetric and volumetric analysis of the samples. Afterward, porosities were evaluated by relating the measured densities to the theoretical density of alumina. To measure the sizing accuracy of the fabricated structures, an optical microscope in combination with an analysis via ImageJ was used. Table 1 lists the parameters that are validated for the accuracy of the 3D-print to obtain identical resonators based on the design in Figure 1. The analysis of the microstructure was done with an SEM (Jeol JSM 7500). For this investigation, the samples were coated with a thin layer of carbon to increase the picture quality, and ImageJ was used to determine the grain size distribution. For the statistical analysis, at least 300 grains were measured for every temperature, and a logarithmic fit was applied to analyze the distribution.

**TABLE 1** Parameters of the fabricated resonator structure.

| Name | Description | Value ($\mu$m) |
|---|---|---|
| $p$ | Hole period | 1160 |
| $h_r$ | Hole radius | 345 |
| $l_x$ | Length in $x$-direction | 12 055 |
| $l_y$ | Length in $y$-direction | 12 760 |
| $h_{s1}$ | Shift of the first hole | 290 |
| $h_{s2}$ | Shift of the two upper holes | 133 |
| $t$ | Shift of the first hole | 789 |

Dielectric properties: The measurement of the *S*-parameters and the analysis of the dielectric photonic crystal properties were performed with two WR-10

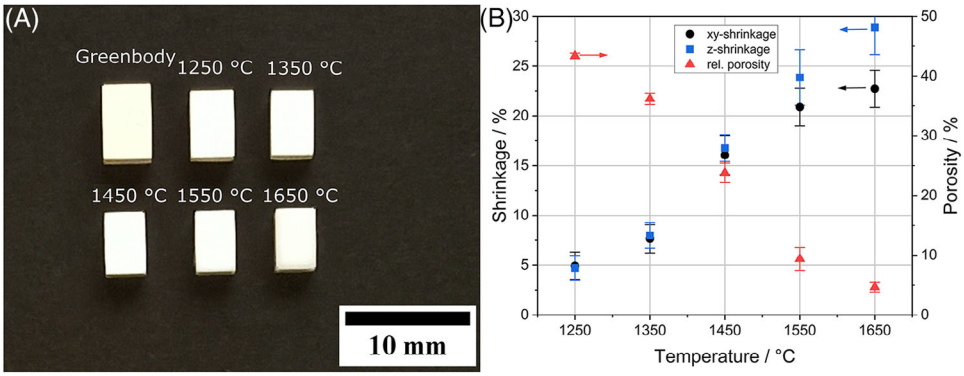


**FIGURE 2** (A) Block green body and blocks sintered at different temperatures from 1250 to 1650°C. (B) Shrinkage and porosity of the sintered blocks as a function of the sintering temperature.

waveguides and a Keysight Technologies N5222A vector network analyzer (VNA). The transmission coefficient, $S_{21}$, is measured via two Anritsu 3740A W-band extensions connected to the VNA. The extraction of material parameters such as material losses is explained in the literature.[19] It must be pointed out that for low-loss materials and particularly for $Al_2O_3$, the difference between simulated and measured *Q*-factors is small, implying that the extraction of the losses can be strongly influenced by misalignment and inaccuracies in the measurement setup. Thus, for a precise estimation of the dielectric sample properties, a high structural accuracy must be ensured, and 10 measurements were performed for each resonator. The set-up for the measurement of the high *Q*-resonator is illustrated in Supplementary A (Figure S2).

## 3 | RESULTS AND DISCUSSION

### 3.1 | Printing optimization

To implement high-Q resonators with identical sizing but different material properties, exact information about the shrinkage factor during thermal post-processing is crucial. Figure 2A shows blocks which were printed with identical sizing and sintered at different temperatures. The higher the sintering temperature, the greater the shrinkage will be. This relationship is illustrated in Figure 2B showing the shrinkage (black and blue) in the sample *x*–*y* (lateral) and *z* (vertical) directions. In comparison with *x*–*y* direction, a greater value is obtained for the *z*-direction. This difference increases with higher sintering temperatures. A possible reason for this could be a different packing factor of the ceramic particles in the green body in *x*–*y* and *z* directions due to the layer-by-layer printing process.[28] Furthermore, the porosity (red) as a function of temperature is illustrated in Figure 2B. During the sintering process, a densification process takes place,[29] leading to a lower porosity at higher temperatures. Apparently, there is a linear dependence with the sintering temperature for both the shrinkage process and the porosity. These results are in good agreement with the literature.[30,31]

With the information summarized in Figure 2B, the fabrication of resonators with identical sizing sintered at different temperatures can be realized. Figure 3A (top) compares the designated green bodies with different sizings to accommodate for the specific shrinkage factors, which results into the anticipated identical sized high-*Q* resonators after thermal post-processing also illustrated in the lower part of Figure 3A. In Supplementary B, examples of microscopic images can be found for every sintering temperature, with the only apparent difference being the presence of light reflections on the surface for higher sintering temperatures. This most likely originates from the difference in ceramic grain size for different sintering temperatures, which will be outlined further in Section 3.3.

As the accuracy of the print has a fundamental significance for the extraction of the dielectric properties, the device parameters from Table 1 were measured for all sintered resonators and analyzed in terms of accuracy. The result of this measurement is plotted in Figure 3B in a normalized form (absolute values are in Supplementary C Table S1). The graph demonstrates that an error of below 2 % was achieved for all analyzed parameters, which proves the accuracy of the shrinkage factors presented in Figure 2B.

### 3.2 | Characterization of the high-*Q* resonators and extraction of materials property

Using the photonic crystal layout discussed in the design section and based on the theoretical material properties of $Al_2O_3$, a resonance frequency of 77 GHz is expected for the resonator sintered at a sintering temperature of

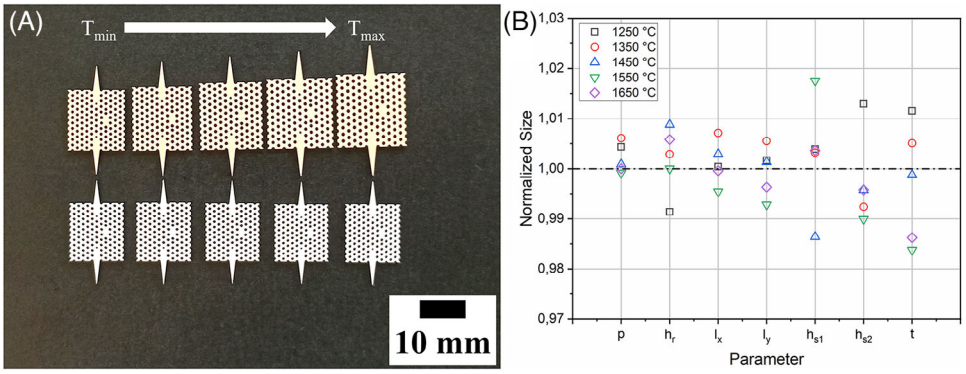


**FIGURE 3** (A) Green bodies (top row) and sintered high-$Q$ resonators (bottom row) made of alumina (left to right: 1250–1650°C). (B) Normalized size of the design parameters for resonators sintered at different temperatures based on Table 1.

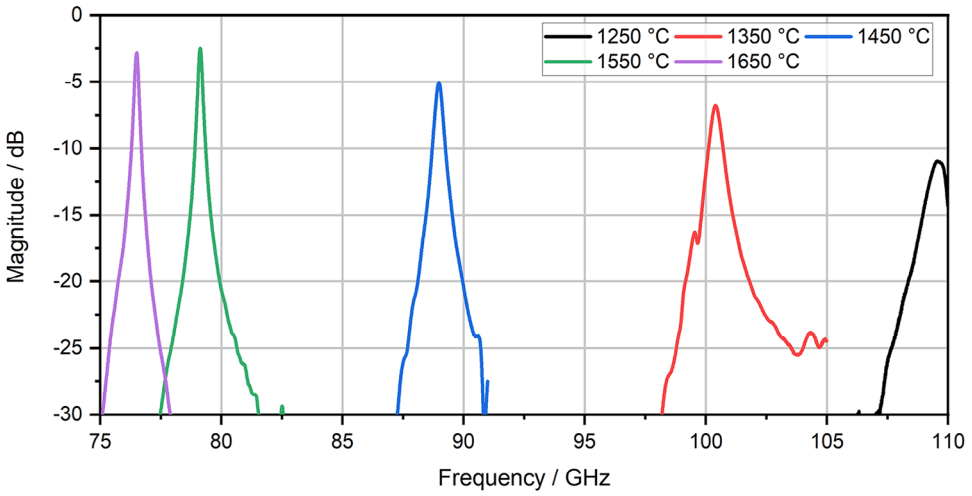


**FIGURE 4** Measurement of the $|S_{21}|$ parameter in dependency of the frequency in the W-band for resonators sintered at different temperatures. For clarity, only the resonance frequency is presented here. The complete measurement for each sintering temperature is depicted in Supplementary D (Figures S8–S12).

$T = 1650°C$. This is confirmed in Figure 4, which illustrates the measured transmission coefficients, $|S_{21}|$, for photonic crystals processed at different sintering temperatures. However, for lower sintering temperatures, a distinct shift of the resonance frequency to higher values is observed from approximately 76.5 GHz (1650°C) up to 109.5 GHz (1250°C). This means that the resonance frequency is shifted in a range of 30 GHz by adjusting the sintering temperature. Thus, the fine adjustment of the resonance frequency and consequently the operation of the device is possible by adjusting the sintering temperature, which otherwise would require redesigning the part or changing the material.[19] A worth noting aspect is the decreasing height and more pronounced width of the resonance peaks as the sintering temperature decreases. As all resonators have identical size, this is caused by a variation of the electrical properties for alumina sintered at different temperatures. It may be concluded that the observed frequency shift is linked to a change in permittivity, whereas the decrease in the transmission coefficient at resonance is attributed to two effects: first, to a weakening of the photonic crystal bandgap due to a lower contrast between the relative permittivity of alumina and air and second, to an increase in dielectric loss with lower sintering temperatures. These parameters are extracted from the measurement as described above in Section 2.3.

The extracted dielectric properties of alumina sintered at different temperature are shown in Figure 5. Figure 5A depicts the resonance frequency as well as the estimated relative permittivity, linking the change in resonance frequency with an increase in relative permittivity. For increasing temperature, the relative permittivity changes from 4.4 at 1250°C to 9.2 at 1650°C. The maximum standard deviation is 0.05 % for the sintering temperature of 1250°C.

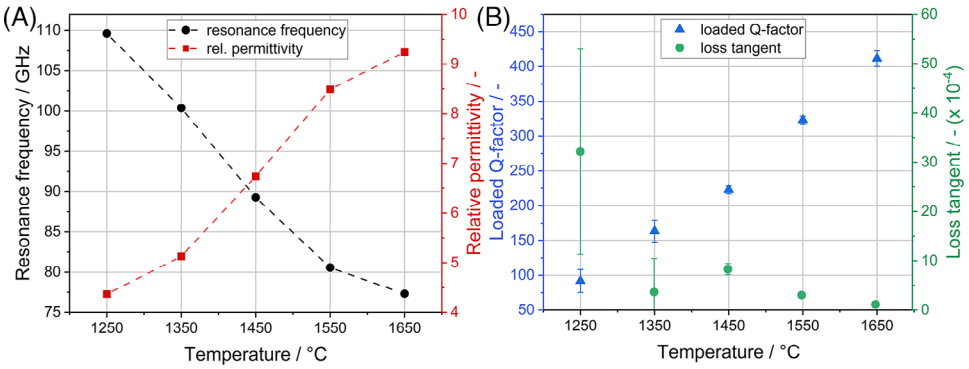


**FIGURE 5** Dielectric properties extracted from the results in Figure 4: (A) Resonance frequency (black) and permittivity (red) and (B) loaded *Q*-factor (blue) and loss tangent (green) are depicted in dependency of the sintering temperature.

Therefore, the measurement of the resonance frequency, and in consequence the estimate of the effective permittivity, is not affected by deviations in the measurement setup.

Figure 5B shows the extracted loaded *Q*-factor and the loss tangent with respect to the temperature. The graph indicates that as the sintering temperature increases, the losses decrease to values in the range of $10^{-4}$, whereas the loaded *Q*-factor increases to respective values in the 400 range. This speaks for the quality of the 3D printed alumina solids. However, the relative standard deviation of the loaded *Q*-factor for the sintering temperatures of 1250 and 1350°C is of 18.02% and 9.77%, respectively. It should be noted that for the case of 1350°C, the extracted losses result in negative values for some measurements, which is physically impossible. These large deviations and nonphysical effects are attributed to the aforementioned weakening of the photonic crystal bandgap. As the permittivity contrast between the evaluated alumina sample and air is lower, the EM wave propagates through the slab and radiates outside of it, instead of being tightly confined in the waveguides and cavity. This implies that the setup, particularly the metallic flanges, strongly influence the measurement results, which is appreciated in the large standard deviation for the sintering temperatures of 1250 and 1350°C. Regardless the average of the extracted losses is still low, with a value of approximately $30 \times 10^{-4}$. This is also confirmed in current literature,[32,33] albeit for lower frequencies.

It should be highlighted that the ability of changing the relative permittivity in the range of 4.4–9.2 while containing low-loss properties is very interesting from a technological point of view. Figure 6 summarizes these results by depicting the relative permittivity and the loss tangent for the evaluated alumina and compares them with conventional low-loss polymer materials for AM. These findings can fill the gap in permittivity mentioned by Rosker et al.[16] for printable materials between 2.5 and 10 and provide

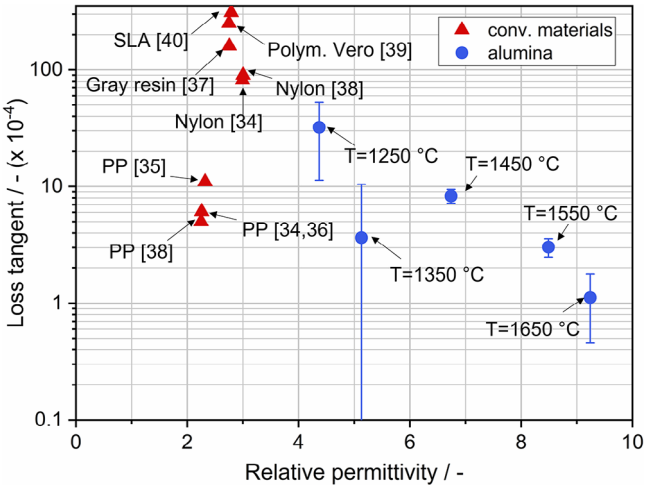


**FIGURE 6** Comparison between loss tangent of conventional low-loss polymer materials for additive manufacturing (AM) and 3D printed alumina samples of this research.[34–40]

a significant benefit for specific device and application designs. Although higher permittivity could be attractive for applications based on total internal reflection,[17] lower permittivity could be interesting for example for Luneburg lenses.[22]

## 3.3 | Effect of microstructure on the material properties

As the investigated samples all have the same final dimensions, the variation in permittivity and dielectric losses due to the sintering temperature is attributed to the change in microstructure (i.e., grain size and porosity) of the material. Figure 7 illustrates SEM images from the different samples sintered at temperatures ranging from $T = 1250°C$ to $T = 1650°C$. The grain size increases significantly with an increase in sintering temperature, which is quantified

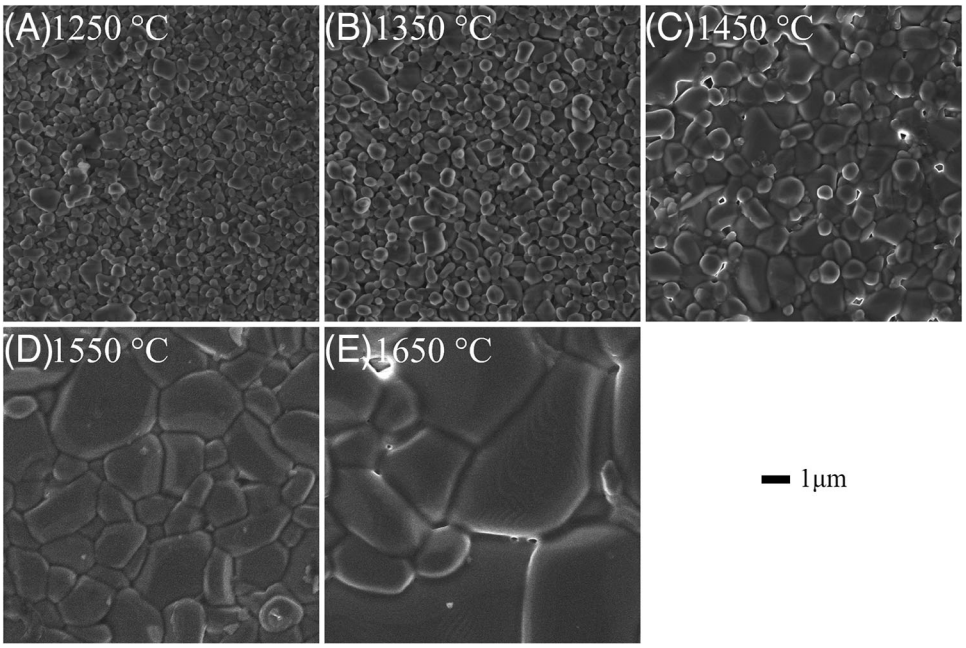


**FIGURE 7** Scanning electron microscopy (SEM) images of the samples sintered at different temperatures (1250°C (A), 1350°C (B), 1450°C (C), 1550°C (D) and 1650°C (E)) with a holding time of 2 h.

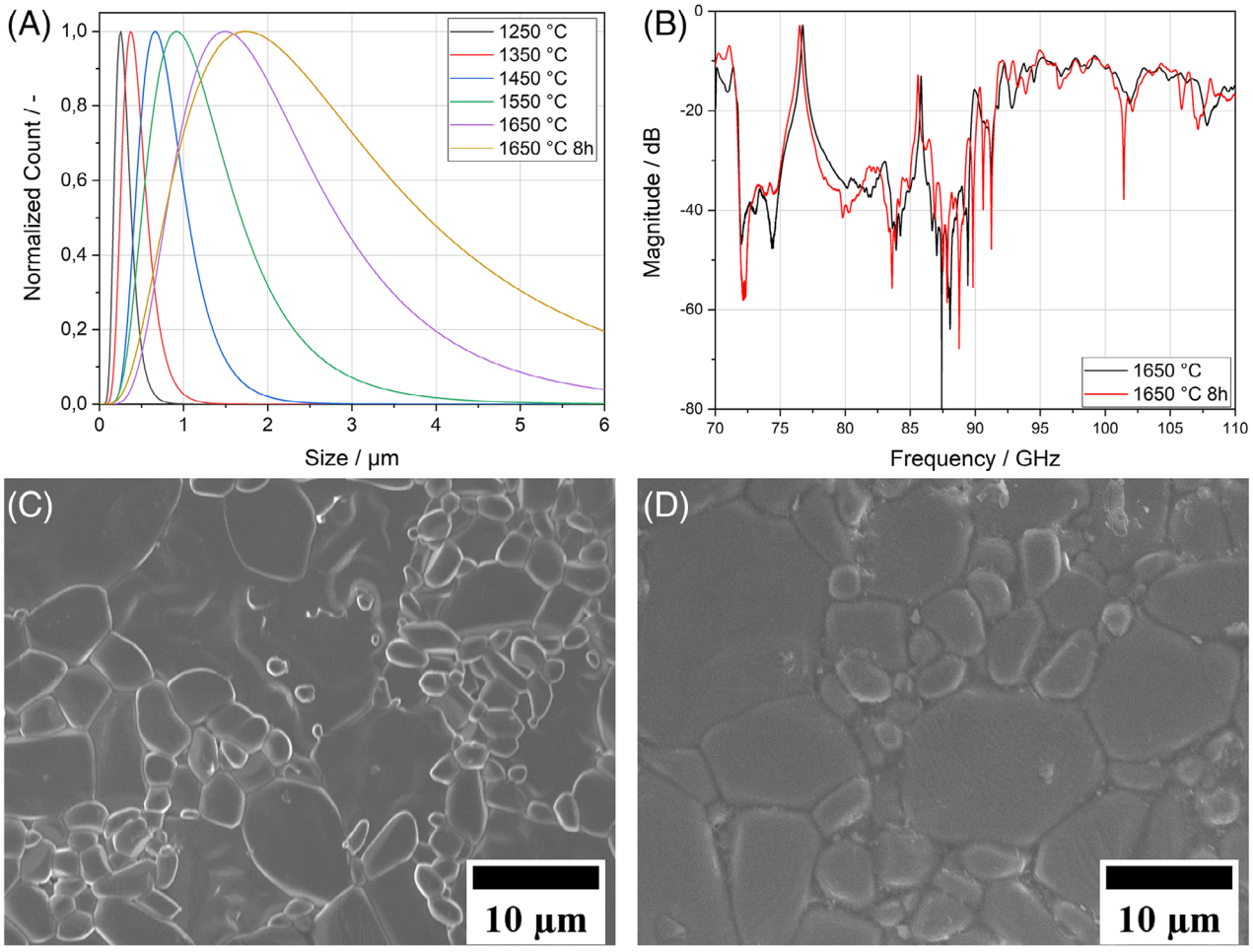


**FIGURE 8** (A) Grain size distribution for different sintering temperatures. (B) $|S_{21}|$ parameters of high-$Q$ resonators sintered at 1650°C with 2 and 8 h holding time. (C) Microstructure of sintered $Al_2O_3$ at 1650°C for 2 h holding time compared to 8 h (D).

in Figure 8A showing the corresponding grain size distributions. At 1250°C, the mean grain size value is 284.4 nm with a geometric standard deviation of $\sigma_g = 1.42$, which increases to a value of 2.01 $\mu$m and $\sigma_g = 1.72$ for a sintering temperature of 1650°C. Thus, not only the average grain size increases exponentially with temperature, but also the width of the distribution function and therefore the scatter or homogeneity of the grain sizes.[41] Figure 7 also illustrates that by increasing the sintering temperature, the porosity of the sample is decreased. This confirms the data shown in Figure 2. As both grain growth and densification occur simultaneously,[29,30] it is difficult to distinguish exactly which parameter has a greater influence on the dielectric properties, which is therefore evaluated in more detail in the following.

### 3.3.1 | Grain size

As Figure 7 illustrates, the densification process is almost completed at high sintering temperatures (e.g., 1650°C). Therefore, this range is suitable for investigating the influence of the grain size in more detail and possibly analyzing it independently of the porosity.[30] For this, two photonic crystal samples sintered at the same max. temperature of $T = 1650$°C; however, processed for different sintering times of 2 and 8 h were considered. Figure 8 summarizes these results by showing the grain size distribution, the measurement of the $|S_{21}|$ parameters, and the SEM images of the two samples. The difference in processing time should lead to a similar sample porosity (i.e., no visible porosity), whereas the change in grain size is significant, as is apparent from Figure 8C,D. The impact of this grain size variation on the $|S_{21}|$ parameter of the photonic crystal is shown in Figure 8B. The resonance frequency of the photonic crystal sintered for an 8 h period is 76.7 GHz, which is only a change of 0.2 GHz to the 2 h sintered sample. This means that a 75% variation in average grain size (3.52 $\mu$m), compared to 2 h holding time (2.01 $\mu$m), corresponds to a 0.26% change in resonance frequency. Therefore, the extracted dielectric properties would only barely change. It is likely that this change in the resonance frequency is the consequence of minor variations in the manufacturing process and that grain size has no significant impact on the dielectric properties in the W-band.

The impact of the grain size on the dielectric sample properties is still under debate in the current literature. One of the ideas is that an increase in grain size, which is in line with a simultaneous decrease in grain boundary density, is associated with a reduction in dielectric loss.[42] However, contradictory results were found, where no influence of grain size on dielectric material losses was observed.[43] Further, especially for high frequencies, the grain size and its size distribution appear to be of minor significance for the dielectric properties,[44] which is in accordance with the findings presented here.

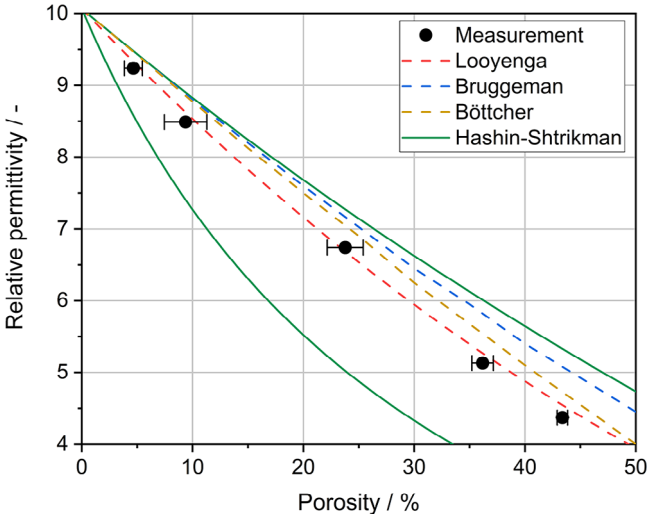


**FIGURE 9** The models of Looyenga, Bruggeman, Böttcher, and Hashin–Shtrikman for the calculation of the relative permittivity in dependency of the mixture content in comparison to the observed data.

**TABLE 2** Applied models to estimate the effective permittivity in dependency of the mixture of two different materials (alumina/air).

| Model name | Description |
|---|---|
| Looyenga[25] (with $\beta = \frac{1}{3}$) | $\varepsilon_{r,eff}{}^{\beta} = \upsilon\, \varepsilon_{r,1}{}^{\beta} + (1-\upsilon)\varepsilon_{r,2}{}^{\beta}$ |
| Bruggeman[24] | $\frac{\varepsilon_{r,eff}-\varepsilon_{r,1}}{2\varepsilon_{r,eff}} = \upsilon \frac{\varepsilon_{r,2}-\varepsilon_{r,1}}{\varepsilon_{r,2}+\varepsilon_{r,eff}}$ |
| Böttcher[23] | $\upsilon = \frac{(\varepsilon_{r,eff}-\varepsilon_{r,1})(2\varepsilon_{r,eff}+\varepsilon_{r,2})}{3\varepsilon_{r,eff}(\varepsilon_{r,2}-\varepsilon_{r,1})}$ |

### 3.3.2 | Porosity

Considering that the observed grain size variation discussed above cannot explain the change in dielectric properties, illustrated in Figure 5, it can be concluded that the porosity is the main factor. Figure 9 illustrates the experimentally determined relative permittivity with respect to the measured porosity (black circles). Further, different models to describe the impact of the porosity on the permittivity are shown. These models are based on calculations using a 2D mixing approach with two dielectric materials shown as the dashed lines. For the calculation of all models, the maximum possible permittivity was assumed to be $\varepsilon_{r,1} = 10.07$ for $Al_2O_3$[43–45] and $\varepsilon_{r,2} = 1$ for air (i.e., porosities). Table 2 summarizes the applied models with $\varepsilon_{r,eff}$ as the effective relative permittivity of the material and $\upsilon$ the volume fraction of alumina in the mixture. Furthermore, an enveloping function is employed based on the model by Hashin–Shtrikman,[46]

which assumes a statistically homogeneous and isotropic mixing of two materials in a three-dimensional space. The enveloping function provides the bounds for the maximum/minimum possible permittivity value. It was originally derived for the description of magnetic permeability; however, the model has been validated for the description of the permittivity.[47]

As Figure 9 shows, the measured relative permittivity data in dependence of the porosity is within the limits of the enveloping function by Hashin–Shtrikman and agrees well with the models of Looyenga, Bruggemann, and Böttcher. This means that for the W-band, the influence of the porosity on the dielectric properties has a more significant impact than the effect of grain size and boundaries, which agrees with the findings of Di Marco et al.,[44] who observed similar effects for frequencies up to 73 GHz.

## 4 | CONCLUSION

In this contribution, the dielectric material properties of additively manufactured alumina were tuned by changing the sample microstructure, using the thermal post processing of the 3D-printed green body. It was substantiated that for W-band frequencies, the relative permittivity and loss tangent are mainly dependent on the material porosity, whereas the grain size distribution can be neglected. Relative permittivity values between 4.4 and 9.2 could be realized by design using a variation in sintering temperature, while maintaining low-loss material properties in the range of $30 \times 10^{-4}$. Therefore, it is expected that this tuneability of the ceramic permittivity will ease the design and manufacturing of 3D-printed ceramic structures for specific applications, while keeping the advantages that ceramic materials typically offer, such as resistance against corrosion, toxic gases, high-temperature stability.

## ACKNOWLEDGMENTS

This work was supported by the German Research Foundation within the project CRC/TRR 196 MARIE, project C09. We acknowledge support by the Open Access Publication Fund of the University of Duisburg-Essen.

Open access funding enabled and organized by Projekt DEAL.

## ORCID

*Masoud Sakaki* https://orcid.org/0000-0001-6238-8360

## REFERENCES

1. Kovacev N, Li S, Li W, Zeraati-Rezaei S, Tsolakis A, Essa K. Additive manufacturing of novel hybrid monolithic ceramic substrates. Aerospace. 2022;9:255.
2. Lakhdar Y, Tuck C, Binner J, Terry A, Goodridge R. Additive manufacturing of advanced ceramic materials. Prog Mater Sci. 2021;116:100736.
3. Jiao C, Xie D, He Z, Liang H, Shen L, Yang Y, et al. Additive manufacturing of bio-inspired ceramic bone scaffolds: structural design, mechanical properties and biocompatibility. Mater Des. 2022;217:110610.
4. Rasaki SA, Xiong D, Xiong S, Su F, Idrees M, Chen Z. Photopolymerization-based additive manufacturing of ceramics: a systematic review. J Adv Ceram. 2021;10:442–71.
5. Praveena BA, Lokesh N, Abdulrajak B, Santhosh N, Praveena BL, Vignesh R. A comprehensive review of emerging additive manufacturing (3D printing technology): methods, materials, applications, challenges, trends and future potential. Mater Today: Proc. 2022;52:1309–13.
6. Misra KP, Misra RDK. Ceramic science and engineering: basics to recent advancements. The Netherlands: Elsevier Science: 2022.
7. He R, Liu W, Wu Z, An D, Huang M, Wu H, et al. Fabrication of complex-shaped zirconia ceramic parts via a DLP- stereolithography-based 3D printing method. Ceram Int. 2018;44:3412–16.
8. An Di, Li H, Xie Z, Zhu T, Luo X, Shen Z, et al. Additive manufacturing and characterization of complex $Al_2O_3$ parts based on a novel stereolithography method. Int J Appl Ceram Technol. 2017;14:836–44.
9. Chen C, Huang B, Liu Z, Li Y, Zou D, Liu T, et al. Additive manufacturing of WC–Co cemented carbides: process, microstructure, and mechanical properties. Addit Manuf. 2023;63:103410.
10. Lin L, Wu H, Ni P, Chen Y, Huang Z, Li Y, et al. Additive manufacturing of complex-shaped and high-performance aluminum nitride-based components for thermal management. Addit Manuf. 2022;52:102671.
11. Wang M, Xie C, He R, Ding G, Zhang K, Wang G, et al. Polymer-derived silicon nitride ceramics by digital light processing based additive manufacturing. J Am Ceram Soc. 2019;102:5117–26.
12. Wei Y, Zhao D, Cao Q, Wang J, Wu Y, Yuan B, et al. Stereolithography-based additive manufacturing of high-performance osteoinductive calcium phosphate ceramics by a digital light-processing system. ACS Biomater Sci Eng. 2020;6:1787–97.
13. O'Masta MR, Stonkevitch E, Porter KA, Bui PP, Eckel ZC, Schaedler T. Additive manufacturing of polymer-derived ceramic matrix composites. J Am Ceram Soc. 2020;103:6712–23.
14. Schwentenwein M, Schneider P, Homa J. Lithography-based ceramic manufacturing: a novel technique for additive manufacturing of high-performance ceramics. In: 13th international ceramics congress—Part B. Switzerland: Trans Tech Publications Ltd; 2014. p. 60–64.
15. Schwentenwein M, Homa J. Additive manufacturing of dense alumina ceramics. Int J Appl Ceram Technol. 2015;12:1–7.
16. Rosker ES, Sandhu R, Hester J, Goorsky MS, Tice J. Printable materials for the realization of high performance RF components: challenges and opportunities. Int J Antennas Propag. 2018;2018:1–19.
17. Jenkel K-D, Sievert B, Rennings A, Sakaki M, Erni D, Benson N. Radar cross-section of ceramic corner reflectors in the W-band fabricated with the LCM-method. IEEE J Radio Freq Identif. 2023:7:278–83.

18. Jenkel K-D, Sievert B, Rennings A, Sakaki M, Erni D, Benson N. Enhanced radar cross-section for W-band corner reflectors using ceramic additive manufacturing. In: *2022 IEEE 12th international conference on RFID technology and applications (RFID-TA)*. New Jersey: IEEE; 2022. p. 37–39.
19. Jimenez-Saez A, Schüßler M, Krause C, Pandel D, Rezer K, Bogel GV, et al. 3D printed alumina for low-loss millimeter wave components. IEEE Access. 2019;7:40719–24.
20. Jimenez-Saez A, Schüßler M, Pandel D, Benson N, Jakoby R. 3D printed 90 GHz frequency-coded chipless wireless RFID tag. In: *2019 IEEE MTT-S international microwave workshop series on advanced materials and processes for RF and THz applications (IMWS-AMP)*. New Jersey: IEEE; 2019. p. 4–6.
21. Jimenez-Saez A, Schüßler M, Krause C, Meyer F, Bögel G, Jakoby R. Photonic crystal THz high-q resonator for chipless wireless identification. In: 2018 First international workshop on mobile terahertz systems (IWMTS). Piscataway, NJ: IEEE; 2018. p. 1–5.
22. Kadera P, Sanchez-Pastor J, Eskandari H, Tyc T, Sakaki M, Schusler M, et al. Wide-angle ceramic retroreflective luneburg lens based on quasi-conformal transformation optics for mm-wave indoor localization. IEEE Access. 2022;10:41097–2011.
23. Böttcher CJF, van Belle OC, Bordewijk P, Rip A. Theory of electric polarization. 2nd ed. Amsterdam: Elsevier; 1973.
24. Bruggeman DAG. Berechnung verschiedener physikalischer konstanten von heterogenen substanzen. I. Dielektrizitätskonstanten und leitfähigkeiten der mischkörper aus isotropen substanzen. Ann Phys. 1935;416:636–64.
25. Looyenga H. Dielectric constants of heterogeneous mixtures. Physica. 1965;31:401–6.
26. T. Burmeister, A. Jiménez-Sáez, M. Sakaki, Schusler M, Sanchez-Pastor J, Benson N, et al. Chipless frequency-coded RFID tags integrating high-Q resonators and dielectric rod antennas. In: *2021 15th European conference on antennas and propagation (EuCAP)*. New Jersey: IEEE; 2021. p. 1–5.
27. Conti L, Bienenstein D, Borlaf M, Graule T. Effects of the layer height and exposure energy on the lateral resolution of zirconia parts printed by lithography-based additive manufacturing. Materials (Basel). 2020;13:1317.
28. Ornik J, Sakaki M, Koch M, Balzer JC, Benson N. 3D printed $Al_2O_3$ for terahertz technology. IEEE Access. 2021;9:5986–93.
29. Gupta TK. Possible correlation between density and grain size during sintering. J Am Ceram Soc. 1972;55:276–77.
30. Rahaman MN. Ceramic processing and sintering. Boca Raton: CRC Press; 2017.
31. Pulgarín HLC, Albano MP. Sintering and microstrusture of $Al_2O_3$ and $Al_2O_3$–$ZrO_2$ ceramics. Procedia Mater Sci. 2015;8:180–89.
32. Mollá J, González M, Vila R, Ibarra A. Effect of humidity on microwave dielectric losses of porous alumina. J Appl Phys. 1999;85:1727–30.
33. Alford NM, Penn SJ. Sintered alumina with low dielectric loss. J Appl Phys. 1996;80:5895–98.
34. Friedsam GL, Biebl EM. Precision free-space measurements of complex permittivity of polymers in the W-band. In: *1997 IEEE MTT-S international microwave symposium digest*. New Jersey: IEEE; 1997. p. 1351–54.
35. Reyes N, Casado F, Tapia V, Jarufe C, Finger R, Bronfman L. Complex dielectric permittivity of engineering and 3D-printing polymers at Q-band. J Infrared Milli Terahz Waves. 2018;39:1140–47.
36. Lamb JW. Miscellaneous data on materials for millimetre and submillimetre optics. Int J Infrared Milli Waves. 1996;17:1997–2034.
37. Duangrit N, Hong B, Burnett AD, Akkaraekthalin P, Robertson ID, Somjit N. Terahertz dielectric property characterization of photopolymers for additive manufacturing. IEEE Access. 2019;7:12339–47.
38. Afsar MN, Moonshiram A, Wang Y. Comparison of millimeter wave dielectric measurement using various techniques. In: *IEEE antennas and propagation society international symposium. Digest held in conjunction with: USNC/CNC/URSI North American radio sci. meeting (Cat. No.03CH37450)*. New Jersey: IEEE; 2003. p. 627–30.
39. Xin H, Liang M. 3-D-printed microwave and THz devices using polymer jetting techniques. Proc. IEEE. 2017;105:737–55.
40. Sahin S, Nahar NK, Sertel K. Dielectric properties of low-loss polymers for mmW and THz Applications. J Infrared Milli Terahz Waves. 2019;40:557–73.
41. Yan MF, Cannon RM, Bowen HK, Chowdhry U. Effect of grain size distribution on sintered density. Mater Sci Eng. 1983;60:275–81.
42. Moreno RM, Requena P, Moya J, Molia JS. Effect of powder characteristics on dielectric properties alumina compacts. 1992.
43. Penn SJ, Alford NM, Templeton A, Wang X, Xu M, Reece M, et al. Effect of porosity and grain size on the microwave dielectric properties of sintered alumina. J Am Ceram Soc. 1997;80:1885–88.
44. Di Marco D, Drissi K, Delhote N, Tantot O, Geffroy PM, Verdeyme S, et al. Dielectric properties of pure alumina from 8 to 73 GHz. J Eur Ceram Soc. 2016;36:3355–61.
45. Vila R, González M, Mollá J, Ibarra A. Dielectric spectro scopy of alumina ceramics over a wide frequency range. J Nucl Mater. 1998;253:141–48.
46. Hashin Z, Shtrikman S. A variational approach to the theory of the effective magnetic permeability of multiphase materials. J Appl Phys. 1962;33:3125–31.
47. Karkkainen KK, Sihvola AH, Nikoskinen KI. Effective permittivity of mixtures: numerical validation by the FDTD method. IEEE Trans Geosci Remote Sensing. 2000;38:1303–8.

## SUPPORTING INFORMATION

Additional supporting information can be found online in the Supporting Information section at the end of this article.

**How to cite this article:** Jenkel K-D, Sánchez-Pastor J, Baloochian MM, Jakoby R, Sakaki M, Jiménez-Sáez A, et al. Effect of sintering temperature on the dielectric properties of 3D-printed alumina ($Al_2O_3$) in the W-band. J Am Ceram Soc. 2024;107:2494–503. https://doi.org/10.1111/jace.19597